Chapter 25

A New Non-Iterative Reconstruction Method for Solving a Class of Inverse Problems

Chapter details

Chapter DOI:

https://doi.org/10.4322/978-65-86503-83-8.c25

Chapter suggested citation / reference style:

Novotny, Antonio A. (2022). “A New Non-Iterative Reconstruction Method for Solving a Class of Inverse Problems”. *In* Jorge, Ariosto B., et al. (Eds.) *Fundamental Concepts and Models for the Direct Problem*, Vol. II, UnB, Brasilia, DF, Brazil, pp. 1007–1023. Book series in Discrete Models, Inverse Methods, & Uncertainty Modeling in Structural Integrity.

P.S.: DOI may be included at the end of citation, for completeness.

Book details

Book: Fundamental Concepts and Models for the Direct Problem

Edited by: Jorge, Ariosto B., Anflor, Carla T. M., Gomes, Guilherme F., & Carneiro, Sergio H. S.

Volume II of Book Series in:

Discrete Models, Inverse Methods, & Uncertainty Modeling in Structural Integrity

Published by: UnB City: Brasilia, DF, Brazil Year: 2022

DOI: https://doi.org/10.4322/978-65-86503-83-8

A New Non-Iterative Reconstruction Method for Solving a Class of Inverse Problems

Antonio André Novotny

Laboratório Nacional de Computação Científica (LNCC), Coordenação de Métodos Matemáticos e Computacionais, Av. Getúlio Vargas 333, 25651-075 Petrópolis - RJ, Brasil. E-mail: novotny@lncc.br

Abstract

Several classes of inverse reconstruction problems are written in the form of over-determined boundary value problems. The general idea consists in rewriting them as an optimization problem. Therefore, a cost functional measuring the misfit between observed and predicted data is minimized with respect to a set of admissible solutions, leading to a non-iterative second order reconstruction algorithm. As a result, the reconstruction process becomes very robust with respect to noisy data and independent of any initial guess. In particular, we are interested in the spatial reconstruction and characterization of (micro-) seismic events via joint source location and moment tensor inversion from pointwise boundary measurements.

Keywords: Topological derivative method, non-iterative reconstruction method, full-waveform inversion, seismic moment tensor, multiple micro-seismic events.

1 Introduction

The topological derivative has been specifically conceived to provide a precise information on the sensitivity of a given shape functional with respect to topological domain perturbations. It appears in the first term of the asymptotic expansion of the shape functional with respect to a small parameter measuring the size of the perturbation under consideration, typically a hole, an inclusion, a source-term, or a crack. See, for instance, the books by Novotny and Sokołowski [2013, 2020].

The origin of the topological derivative method in optimal design can be dated to the work by Schumacher [1995] on the optimal location of holes within elastic structures. It is nevertheless worth mentioning prior related mathematical developments on the asymptotic behaviour of solutions to singularly perturbed boundary value problems and on the notions of polarization and capacity matrices. These objects are essential ingredients in the formulation of topological derivatives. The first mathematical justifications for topological derivatives in the framework of partial differential equations are due Sokołowski and Żochowski [1999] and Garreau et al. [2001], in the context of the Poisson equation and the Navier system for Neumann and Dirichlet holes.

In the last decade, the topological sensitivity analysis has become a rich and fascinating research field that combines the modern theory of calculus of variations, partial differential equations, differential geometry, numerical analysis, physics, engineering and computational mechanics. The field grew up rapidly to develop many extensions and address a variety of physical and industrial problems. The topological derivative method has applications in shape and topology optimization [Novotny et al., 2007, Amstutz and Novotny, 2010], inverse problems [Canelas et al., 2015, Ferreira and Novotny, 2017], image processing [Auroux et al., 2007, Amstutz et al., 2014], multi-scale material design [Amstutz et al., 2010, Giusti et al., 2010] and mechanical modelling, including damage [Allaire et al., 2011] and fracture [Xavier et al., 2017] evolution phenomena. See, for instance, the book by Novotny et al. [2019a] and the special issue on the topological derivative method and its applications in computational engineering recently published in the Engineering Computations Journal [Novotny et al., 2022], covering various topics ranging from new theoretical developments [Amstutz, 2022, Baumann and Sturm, 2022, Delfour, 2022] to applications in structural and fluid dynamics topology optimization [Kliewe et al., 2022, Romero, 2022, Santos and Lopes, 2022], geometrical inverse problems [Bonnet, 2022, Canelas and Roche, 2022, Fernandez and Prakash, 2022, Louër and Rapún, 2022a,b] synthesis and optimal design of metamaterials [Ferrer and Giusti, 2022, Yera et al., 2022], fracture mechanics modelling [Xavier and Van Goethem, 2022], up to industrial applications [Rakotondrainibe et al., 2022] and experimental validation of the topological derivative method [Barros et al., 2022].

In this chapter, we are interested in the spatial reconstruction and characterization of (micro-) seismic events via joint source location and moment tensor inversion from pointwise boundary measurements. Seismic and micro-seismic source characterization is a keen area of research in geophysics, engineering, hydrocarbon production, and materials science due to its central role in the understanding of earthquake and faulting processes [Shearer, 2009]; monitoring of mines, highway bridges, and offshore platforms [Koerner et al., 1981]; tracking the progress of hydraulic fracturing [Baig and Urbancic, 2010], and investigating the failure of brittle materials [Grosse and Ohtsu, 2008]. Generally speaking any (micro-) seismic source, interpreted as a sudden material failure, can be characterized by its spatial support, temporal variation, and the underpinning failure mechanism. In situations when the extent of a material failure is small relative to the remaining length scales in the problem (e.g. seismic wavelengths and source-receiver distances), the seismic source can be interpreted as a point source [Scruby et al., 1985, Jost and Herrmann, 1989]; a hypothesis that is implicitly assumed hereon. In this setting, the accepted continuum mechanics description of a seismic source is given by a linear combination of force dipoles [Aki and Richards, 2009] whose weights are specified in terms of the so-called *seismic moment tensor* [Gilbert, 1973]; a second-order tensorial quantity whose accurate reconstruction from remote wavefield measurements is the key point of seismic source characterization.

In contrast to the classical approaches to moment tensor inversion in laboratory [Scruby et al., 1985] and geophysical [Jost and Herrmann, 1989] environments that rely on prior knowledge of the source location and possibly other simplifying assumptions (e.g. far field hypothesis), recent attempts at seismic source characterization are increasingly based on the full waveform analysis of multi-axial seismic observations [Cesca and Dahm, 2008]. In general, the latter can be pursued either via time- or frequency-domain approaches. As an example of the former class of inverse solutions, the paper by Song and Toksöz [2011] deploys grid search for the source location – aiming to minimize the misfit between the observed and synthetic waveforms, followed by a least-squares solution for the moment tensor that relies on an *a priori* premise of the source time function. In the paper by Sjögreen and Petersson [2014], on the other hand, the investigators pursue simultaneous inversion for the source location, moment tensor, and two-parameter source time function via nonlinear minimization of the germane waveform misfit, aided by adjoint-field sensitivity estimates. In recent years, studies by Bazargani and Snieder [2015] and Kawakatsu and Montagner [2008] have demonstrated the utility of time reversal methods as a viable (time- or frequency-domain) alternative for exposing the seismic source location. With the latter information at hand, a full-waveform reconstruction of the moment tensor, including the underpinning source time function, can be conveniently pursued in the frequency domain [Cesca and Dahm, 2008] by solving the underpinning linear system of equations.

A common thread to the above and related inverse source analyses entails (i) the fundamental premise of a *synchronous seismic source*, where all components of its moment tensor share the same time dependence (given by the source time function); and (ii) the assumption of *a single* seismic (point) source, precluding the possibility that two events – originating from distinct locations – may overlap in time. To provide an alternative to the foregoing analyses that is free of such impediments, this work deals with spatial reconstruction and characterization of micro-seismic events in the frequency domain from pointwise wavefield measurements, where the associated moment tensors are fully reconstructed. Since the inverse problem at hand is (as expected) ill-posed, the idea is to rewrite it as an optimization problem in which a functional measuring the misfit between synthetic and observed waveforms is minimized with respect to a set of admissible point sources representing the hidden faults. The necessary optimality conditions are derived in the spirit of the topological derivative method as proposed by Novotny et al. [2019b] which, in this context, consists in exposing the perturbation of the functional as a quadratic function of the germane moment tensor components. Then, the resulting expansion is trivially minimized with respect to the sought source parameters, leading to a non-iterative reconstruction algorithm that is initial guess-free and robust with respect to perturbations of sensory data. We test the proposed technique via numerical experiments designed to examine its performance under a variety of source, sensing, and uncertainty scenarios.

The chapter is organized as follows. The germane (frequency-domain) forward problem and affiliated inverse problem, targeting the locations and moment-tensor "strengths" of micro-seismic events from the observed acoustic emission data, are described in Section 2. In Section 2.1 the germane cost functional, measuring the misfit between the synthetic and sensory data, is expanded with respect to the set of admissible source densities. The resulting expansion is used to devise a novel reconstruction algorithm presented in Section 2.2. A set of numerical experiments examining the effectiveness of the proposed reconstruction algorithm is provided in Section 3. Finally, the chapter ends with some concluding remarks presented in Section 4.

2 Full-Waveform Inversion of Seismic Moment Tensors

Following the original ideas presented in the paper by Amad et al. [2020], let us consider an open and bounded domain $\Omega \subset \mathbb{R}^2$ representing an elastic body. Its boundary is denoted as $\partial\Omega$, such that $\Gamma_N \subset \partial\Omega$ and $\Gamma_D = \partial\Omega \setminus \Gamma_N$ denote respectively the parts of $\partial\Omega$

subjected to homogeneous Neumann and Dirichlet boundary conditions. In this setting, we are interested in the inverse source problem of reconstructing the source density f^* such that

$$\begin{cases} -\mathrm{div}\sigma(u) - \rho\omega^2 u &= f^* \quad \text{in} \quad \Omega, \\ u &= u^* \quad \text{on} \quad \Gamma_m \subset \Gamma_N, \\ u &= 0 \quad \text{on} \quad \Gamma_D, \\ \sigma(u)n &= 0 \quad \text{on} \quad \Gamma_N, \end{cases} \tag{1}$$

where $u : \Omega \to \mathbb{R}^2$ is the elastodynamic displacement field; ω denotes the frequency of wave motion; ρ is the density; n is the unit outward normal on $\partial\Omega$; $\Gamma_m \subset \Gamma_N$ is the measurement surface; and u^* are the acoustic emission data from which we aim to resolve f^*. See Fig. 1. In addition, $\sigma(u) = \mathbb{C}(\nabla u)^s$ is the Cauchy stress tensor, with $\mathbb{C}$ the elasticity tensor and $(\cdot)^s$ the symmetric part of a second order tensor $(\cdot)$. Without loss of generality, we assume the elastic body Ω to be homogeneous and isotropic, in which case the elasticity tensor reads

$$\mathbb{C} = 2\mu\,\mathbb{I} + \lambda(\mathrm{I} \otimes \mathrm{I}), \tag{2}$$

where λ and μ are the Lamé moduli, and $\mathbb{I}$ and I are the fourth and second order identity tensors, respectively. The source density $f^* \in C_\delta(\Omega)$ to be reconstructed is given by a superposition of a finite number of dipoles, where

$$C_\delta(\Omega) = \Big\{ f : \Omega \to \mathbb{R}^2 \mid f(x) = \sum_{i=1}^{N} M_i \nabla_{x_i} \delta(x - x_i) \Big\}. \tag{3}$$

Here, $\delta(\cdot)$ is the two-dimensional Dirac delta function; N denotes the number of point sources located at $x_i \in \Omega$ $(i = 1, 2, \ldots, N)$, and $M_i \in \mathbb{R}^2 \times \mathbb{R}^2$ is a symmetric seismic moment tensor characterizing the i-th point source. For completeness, we recall from the continuum mechanics definition [Aki and Richards, 2009] that a generic seismic moment tensor is represented as

$$M = a\,\mathbb{C}([\![u]\!] \odot \eta), \tag{4}$$

where a is the area of a newly created micro-fracture (giving rise to the acoustic emission) whose unit normal is denoted by η, and $[\![u]\!]$ is the average displacement jump across the micro-fracture. Finally, $u \odot v$ denotes the symmetric tensor product between the vectors u and v, namely $u \odot v = \frac{1}{2}(u \otimes v + v \otimes u)$. On the basis of (3), we write the sought source density satisfying (1) as

$$f^*(x) = \sum_{i=1}^{N^*} M_i^* \nabla_{x_i^*} \delta(x - x_i^*). \tag{5}$$

Now, let us rewrite the inverse problem (1) as an optimization problem. The associated functional to be minimized in $C_\delta(\Omega)$ is given by

$$\mathcal{J}(u) := \frac{1}{2} \int_{\Gamma_m} \|u - u^*\|^2, \tag{6}$$

where $u : \Omega \to \mathbb{R}^2$ solves the boundary value problem

$$\begin{cases} -\mathrm{div}\sigma(u) - \rho\omega^2 u &= f \quad \text{in} \quad \Omega, \\ u &= 0 \quad \text{on} \quad \Gamma_D, \\ \sigma(u)n &= 0 \quad \text{on} \quad \Gamma_N, \end{cases} \tag{7}$$

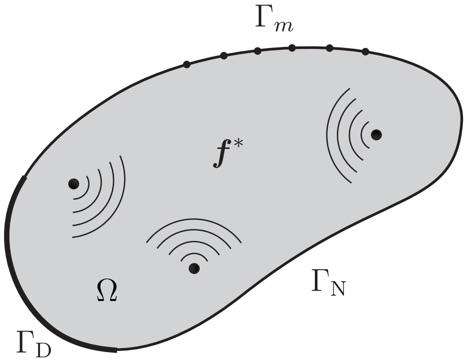

Figure 1: Problem setting.

for a trial source term $f \in C_\delta(\Omega)$. In this setting, the relevant optimization problem can be stated as

$$\underset{f \in C_\delta(\Omega)}{\text{Minimize}}\ \mathcal{J}(u), \text{ subject to (7).} \tag{8}$$

2.1 Sensitivity Analysis

The next step is to minimize the misfit functional (6) with respect to the set of admissible solutions (3). In order to evaluate the germane sensitivities of this functional, the idea is to perturb the trial source term $f \in C_\delta(\Omega)$ in (7) by a fixed number N of point sources with arbitrary locations x_i and generic moment tensors M_i as

$$f_\delta(x) = f(x) + \sum_{i=1}^{N} M_i \nabla_{x_i} \delta(x - x_i), \tag{9}$$

where $M_i \in \mathbb{R}^2 \times \mathbb{R}^2$ are symmetric. On the basis of (7) and (9), we can introduce the forward solution $u_\delta : \Omega \to \mathbb{R}^2$ as that solving

$$\left\{ \begin{array}{rcll} -\text{div}\sigma(u_\delta) - \rho\omega^2 u_\delta &=& f_\delta & \text{in} \quad \Omega, \\ u_\delta &=& 0 & \text{on} \quad \Gamma_D, \\ \sigma(u_\delta)n &=& 0 & \text{on} \quad \Gamma_N, \end{array} \right. \tag{10}$$

which gives rise to the perturbed cost functional

$$\mathcal{J}(u_\delta) = \frac{1}{2} \int_{\Gamma_m} \|u_\delta - u^*\|^2. \tag{11}$$

Assuming a sufficient number of micro-seismic source locations x_i ($i = 1, 2, \ldots, N$), we are interested in obtaining the variation of (6) with respect to the components of the moment tensor M_i at each location. To facilitate the analysis, one may decompose M_i into its Cartesian components using Einstein summation notation over repeated indexes $k, l = 1, 2$, namely

$$M_i = M_i^{kl}(e_k \otimes e_l), \tag{12}$$

where e_k and e_l are the unit vectors of the reference Cartesian frame, and M_i^{kl} are the components of M_i. With such definitions, the solution of (10) can be conveniently decomposed as

$$u_\delta(x) = u(x) + \sum_{i=1}^{N} M_i^{kl} p_i^{kl}(x), \tag{13}$$

where $p_i^{kl} : \Omega \to \mathbb{R}^2$ solve the canonical boundary value problems of the form

$$\left\{ \begin{array}{rcll} -\mathrm{div}\sigma(p_i^{kl}) - \rho\omega^2 p_i^{kl} &=& (e_k \otimes e_l)\nabla_{x_i}\delta(x - x_i) & \text{in} \quad \Omega, \\ p_i^{kl} &=& 0 & \text{on} \quad \Gamma_D, \\ \sigma(p_i^{kl})n &=& 0 & \text{on} \quad \Gamma_N, \end{array} \right. \tag{14}$$

for $k, l = 1, 2$. Here it is useful to note that, thanks to ansatz (13), canonical problems (14) are independent of the components M_i^{kl} of the moment tensor M_i in (12). Now we have all elements needed to evaluate the variation of functional (6) with respect to M_i^{kl}. Specifically, on substituting (13) in (11), we obtain

$$\mathcal{J}(u_\delta) = \mathcal{J}(u) + \sum_{i=1}^{N} M_i^{kl} \int_{\Gamma_m} p_i^{kl} \cdot (u - u^*) + \frac{1}{2} \sum_{i=1}^{N} \sum_{j=1}^{N} M_i^{kl} M_j^{mn} \int_{\Gamma_m} p_i^{kl} \cdot p_j^{mn}, \tag{15}$$

assuming implicit summation over repeated indexes $k, l, m, n = 1, 2$.

For a systematic treatment of (15), we next introduce the vector of trial source locations

$$\xi = (x_1, x_2, \ldots, x_N) \in \mathbb{R}^{2N} \tag{16}$$

and the affiliated strength vectors

$$\alpha = (\alpha_1, \alpha_2, \ldots, \alpha_N)^\top \in \mathbb{R}^{3N}, \tag{17}$$

collecting the respective components of M_i, where

$$\alpha_i = (M_i^{11}, M_i^{22}, M_i^{12} = M_i^{21})^\top .$$

With such definitions, the residual in (15) can be rewritten more compactly as

$$\begin{aligned} \Psi(\alpha) &:= \mathcal{J}(u_\delta) - \mathcal{J}(u) && (18) \\ &= h \cdot \alpha + \frac{1}{2} H\, \alpha \cdot \alpha. && (19) \end{aligned}$$

Here, vector $h \in \mathbb{R}^{3N}$ and matrix $H \in \mathbb{R}^{3N} \times \mathbb{R}^{3N}$ are respectively defined as

$$h := \begin{pmatrix} h_1 \\ h_2 \\ \vdots \\ h_N \end{pmatrix}, \quad \text{and} \quad H := \begin{pmatrix} H_{11} & H_{12} & \ldots & H_{1N} \\ H_{21} & H_{22} & \ldots & H_{2N} \\ \vdots & \vdots & \ddots & \vdots \\ H_{N1} & H_{N2} & \ldots & H_{NN} \end{pmatrix}, \tag{20}$$

whose entries are given by

$$h_i := \begin{pmatrix} h_i^1 \\ h_i^2 \\ h_i^3 \end{pmatrix}, \quad \text{and} \quad H_{ij} := \begin{pmatrix} H_{ij}^{11} & H_{ij}^{12} & \ldots & H_{ij}^{13} \\ H_{ij}^{21} & H_{ij}^{22} & \ldots & H_{ij}^{23} \\ H_{ij}^{31} & H_{ij}^{32} & \ldots & H_{ij}^{33} \end{pmatrix}, \tag{21}$$

where

$$h_i^1 := \int_{\Gamma_m} p_i^{11} \cdot (u - u^*), \quad h_i^2 := \int_{\Gamma_m} p_i^{22} \cdot (u - u^*), \quad h_i^3 := \int_{\Gamma_m} (p_i^{12} + p_i^{21}) \cdot (u - u^*),$$

and

$$\begin{aligned}
H_{ij}^{11} &:= \int_{\Gamma_m} p_i^{11} \cdot p_j^{11}, \quad H_{ij}^{12} := \int_{\Gamma_m} p_i^{11} \cdot p_j^{22}, \quad H_{ij}^{13} := \int_{\Gamma_m} p_i^{11} \cdot (p_j^{12} + p_j^{21}),\\
H_{ij}^{21} &:= \int_{\Gamma_m} p_i^{22} \cdot p_j^{11}, \quad H_{ij}^{22} := \int_{\Gamma_m} p_i^{22} \cdot p_j^{22}, \quad H_{ij}^{23} := \int_{\Gamma_m} p_i^{22} \cdot (p_j^{12} + p_j^{21}),\\
H_{ij}^{31} &:= \int_{\Gamma_m} (p_i^{12} + p_i^{21}) \cdot p_j^{11}, \quad H_{ij}^{32} := \int_{\Gamma_m} (p_i^{12} + p_i^{21}) \cdot p_j^{22},\\
H_{ij}^{33} &:= \int_{\Gamma_m} (p_i^{12} + p_i^{21}) \cdot (p_j^{12} + p_j^{21}).
\end{aligned}$$

2.2 Reconstruction Algorithm

For each fixed pair (N, ξ), we seek α that minimizes Ψ according to (19). Since Ψ represents a quadratic form with respect to α, sufficient optimality condition

$$\langle D_\alpha \Psi(\alpha), \delta\alpha \rangle = 0, \quad \forall\, \delta\alpha \in \mathbb{R}^{3N}, \tag{22}$$

lead to the linear system

$$H\alpha = -h. \tag{23}$$

In this setting, the solution α of (23) is implicitly a function of the vector (16) of source locations ξ, namely $\alpha = \alpha(\xi)$. On substituting (23) into (19), the optimal vector of source locations $\xi^\star$ can be trivially obtained via combinatorial search over a prescribed grid, X, of $M \geqslant N$ trial source locations geared toward solving the minimization problem

$$\xi^\star = \underset{\xi \subset X}{\operatorname{argmin}} \left\{ \Psi(\alpha(\xi)) = \frac{1}{2} h \cdot \alpha(\xi) \right\}. \tag{24}$$

On resolving $\xi^\star$, the components of N reconstructed moment tensors $M_i^\star$ are then given by the optimal strength vector $\alpha^\star = \alpha(\xi^\star)$. The associated optimal value of the objective function is denoted as $\Psi^\star := \Psi(\alpha^\star)$. We remark that when the true number of micro-seismic sources, $N^\star$, is less than N, numerical simulations show that a number $N - N^\star$ of components $\alpha_i^\star$, in the solution set $\alpha^\star$, take near-trivial values.

To complete the analysis, we next introduce a second-order optimization algorithm that synthesizes the process of obtaining $\xi^\star$ and $\alpha^\star$ from the computational point of view. The input of the algorithm is listed below:

- Upper bound N on the number of (micro-seismic) point sources.
- Grid X of $M \geqslant N$ trial source locations.
- Canonical solutions p_i^{kl} for each grid point $x_i \in X$.

Algorithm 1: Micro-seismic source reconstruction

input : $N, X, p_i^{kl}\ \forall x_i \in X$

Initialization: $\xi^\star \leftarrow 0$; $\alpha^\star \leftarrow 0$; $\Psi^\star \leftarrow \infty$; $M \leftarrow \text{card}(X)$

for $i_1 \leftarrow 1$ **to** M **do**

  for $i_2 \leftarrow i_1 + 1$ **to** M **do**

    $\vdots$

    for $i_N \leftarrow i_{N-1} + 1$ **to** M **do**

$$h \leftarrow \begin{bmatrix} h_{(i_1)} \\ h_{(i_2)} \\ \vdots \\ h_{(i_N)} \end{bmatrix}; \quad H \leftarrow \begin{bmatrix} H_{(i_1 i_1)} & H_{(i_1 i_2)} & \cdots & H_{(i_1 i_N)} \\ H_{(i_2 i_1)} & H_{(i_2 i_2)} & \cdots & H_{(i_2 i_N)} \\ \vdots & \vdots & \ddots & \vdots \\ H_{(i_N i_1)} & H_{(i_N i_2)} & \cdots & H_{(i_N i_N)} \end{bmatrix}$$

      $\alpha \leftarrow -H^{-1}h$; $\Psi \leftarrow \frac{1}{2} h \cdot \alpha$

      $\mathcal{I} \leftarrow (i_1, i_2, \ldots, i_N)$; $\quad \xi \leftarrow \Pi(\mathcal{I})$

      if $\Psi < \Psi^\star$ **then**

        $\xi^\star \leftarrow \xi$; $\quad \alpha^\star \leftarrow \alpha$; $\quad \Psi^\star \leftarrow \Psi$

      end if

    end for

  end for

end for

return $\xi^\star$, $\alpha^\star$, $\Psi^\star$

The algorithm returns the optimal set of source locations $\xi^\star$ and respective moment tensor components given by $\alpha^\star$. The above procedure, originally developed in the paper by Canelas et al. [2014] in the context of inverse potential problems, is shown in Algorithm 1 using pseudo-code format. Therein, $\Pi : \{1, 2, \ldots, M\}^N \mapsto X$ maps the vector of source indices $\mathcal{I} = (i_1, i_2, \ldots, i_N)$ to the corresponding vector of source locations $\xi \subset X$. For further applications of this algorithm, we refer to the paper by Novotny et al. [2019b].

In Algorithm 1, optimal source locations $\xi^\star$ are obtained through a combinatorial search over M trial points sampling the set of admissible locations X. As a result, the computational complexity $\mathcal{C}(M, N)$ of the algorithm can be evaluated by the formula

$$\mathcal{C}(M, N) \approx \begin{pmatrix} M \\ N \end{pmatrix} N^3 = \frac{M!}{N!(M-N)!} N^3.$$

In Fig. 2, the graphs of $N \times \log_{10}(\mathcal{C}(M, N))$ for $M = 100$ and $M = 400$ are plotted as solid and dashed lines, respectively. As can be seen from the display, the computational cost of the algorithm may become prohibitive for a large N, with $N \approx M/2$. In the ensuing numerical examples (Section 3), we set $N \ll M$, so that Algorithm 1 runs in a few seconds for all examples.

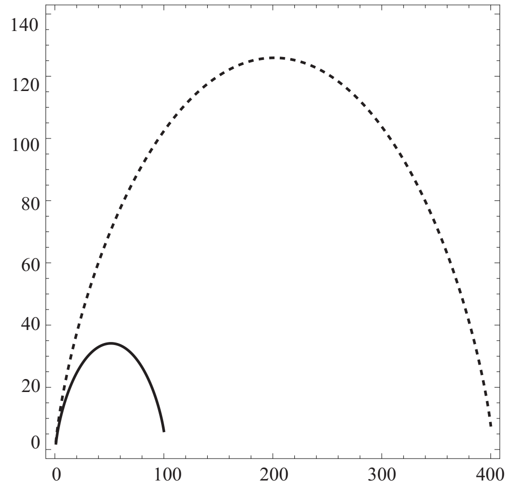

Figure 2: Complexity order of Algorithm 1: $N \times \log_{10}(\mathcal{C}(M, N))$ **for** $M = 100$ **(solid) and** $M = 400$ **(dashed).**

3 Numerical Results

Thanks to the fact that the moment tensor $M_i \in \mathbb{R}^2 \times \mathbb{R}^2$ is symmetric, its eigenvalues can be conveniently written as

$$m_i^{1,2} := \frac{1}{2}\left(\operatorname{tr}(M_i) \pm \sqrt{M_i^D \cdot M_i^D}\right) \tag{25}$$

in terms of the volumetric $\operatorname{tr}(M_i)$ and deviatoric M_i^D components of M_i, with

$$M_i^D = M_i - \frac{1}{2}\operatorname{tr}(M_i)\mathrm{I}. \tag{26}$$

In the sequel, we denote the affiliated eigenvectors by $v_i^{1,2}$.

For the purposes of source inversion, we next consider three types of micro-seismic events given by the moment tensors $M_i^* \in \mathbb{R}^2 \times \mathbb{R}^2$ ($i = 1, \ldots, N^*$) featuring [Aki and Richards, 2009]: (i) real amplitude $\gamma_i \in \mathbb{R}$, (ii) unit normal to the micro-crack $\eta_i \in \mathbb{R}^2$ (when applicable), and (iii) Lamé moduli μ and λ of the background solid. Specifically, when generating the synthetic data u^* according to (1) and (5), we allow for

1. Cavitation:
$$M_i^* = 2\gamma_i(\mu + \lambda)\mathrm{I} \quad \Rightarrow \quad m_i^{1,2} = 2\gamma_i(\mu + \lambda); \tag{27}$$

2. Mode I crack:
$$M_i^* = \gamma_i(2\mu(\eta_i \otimes \eta_i) + \lambda\mathrm{I}) \quad \Rightarrow \quad m_i^1 = \gamma_i(2\mu + \lambda),\ m_i^2 = \gamma_i\lambda; \tag{28}$$

3. Mode II crack:
$$M_i^* = \gamma_i\mu(\eta_i^\perp \otimes \eta_i + \eta_i \otimes \eta_i^\perp) \quad \Rightarrow \quad m_i^{1,2} = \pm\gamma_i\mu. \tag{29}$$

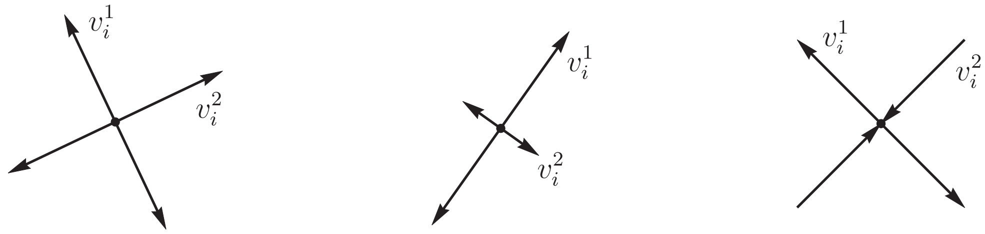

(a) $m_i^1 = m_i^2 > 0$ (b) $m_i^1 > m_i^2 > 0$ (c) $m_i^1 > 0 > m_i^2$

Figure 3: Representation of the moment tensors in terms of their eigenvalues and eigenvectors: (a) cavitation, (b) mode I crack, and (c) mode II crack.

For future reference, the moment tensors given by (27)–(29) are depicted graphically in Fig. 3.

The elastic body Ω used for numerical simulations is taken as an $\ell \times \ell$ block of rock with mass density ρ and Lamé moduli $\lambda = \mu$ (Poisson's ratio $\nu = 0.25$), fixed at the bottom corners. The pointwise motion sensors are assumed to be distributed along the boundary $\partial\Omega$ with various densities and apertures as described in the sequel. The dimensionless frequency of acoustic emission is taken as

$$\bar{\omega} = \frac{\omega\,\ell}{\sqrt{\mu/\rho}} = 10\pi,$$

resulting in the specimen-size-to-shear-wavelength ratio of $\ell/\lambda_s = 5$. With reference to (4), (9) and (27)–(29), we also introduce the dimensionless coordinates $y = \ell^{-1}x$; we consider the dimensionless source strength $\bar{\gamma} = \ell^{-3}\gamma$, and we specify the unit normal to the micro-crack as $\eta = (\cos\theta, \sin\theta)$, where θ is the angle measured counterclockwise from the horizontal axis. The forward elastodynamic problem is solved via standard Galerkin finite element method. To handle the germane wave propagation with sufficient accuracy, domain Ω is first subdivided into a uniform 10×10 grid of square subdomains. Then, each subdomain is discretized via 4^n triangular finite elements with $n = 7$. Next, the set of admissible source locations X is taken as the union of vertices of like triangles with $n = 1$, giving $M = 221$ in Algorithm 1. Finally, the dipoles are represented by a Gaussian distribution of the form

$$\delta(x - x_i) = \lim_{\varepsilon\to 0} \frac{1}{2\pi\varepsilon^2} \exp\left(-\frac{\|x - x_i\|^2}{2\varepsilon^2}\right). \tag{30}$$

The gradient of $\delta(x - x_i)$ with respect to x_i can be obtained as follows

$$\nabla_{x_i}\delta(x - x_i) = \lim_{\varepsilon\to 0} \frac{x - x_i}{2\pi\varepsilon^4} \exp\left(-\frac{\|x - x_i\|^2}{2\varepsilon^2}\right), \tag{31}$$

where the parameter $\varepsilon = 10^{-2} \times h^e$ for the numerical purposes, with h^e used to denote the size of the finite element.

To illustrate the performance of the inversion algorithm, we adopt the graphical representation of moment tensors introduced in Fig. 3, and we denote the true (resp. reconstructed) sources by thick red (resp. thin blue) arrows. Finally, the pointwise sensors are represented by black dots.

3.1 Example 1

In this example, we pursue reconstruction of one, two and three micro-seismic sources representing: (i) cavitation, (ii) mode I and mode II cracks and (iii) cavitation, mode I and mode II cracks. More precisely, in Fig. 4 there are: (a) $\bar{\gamma}_1 = 0.02$; (b) $\bar{\gamma}_1 = 0.04$ and $\theta_1 = 20°$, $\bar{\gamma}_2 = 0.01$ and $\theta_2 = 15°$; and (c) $\bar{\gamma}_1 = 0.01$, $\bar{\gamma}_2 = 0.03$ and $\theta_2 = 20°$, $\bar{\gamma}_3 = 0.02$ and $\theta_3 = 15°$. As sensory data, we consider the biaxial motion measurements captured by one, two and three pairs of sensors, respectively. As expected, the sources reconstructions shown in Fig. 4 are nearly exact in all cases.

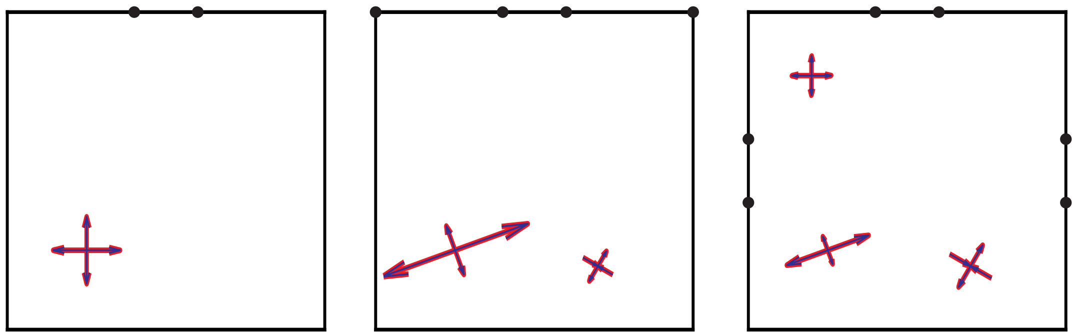

(a) single micro-fault (b) two micro-faults (c) three micro-faults

Figure 4: Reconstruction of one, two and three micro-faults using different configurations of biaxial motion sensors.

At this point, it is worth noting that the reconstruction fails if a smaller-than-featured number of sensors is deployed in each of the foregoing examples. Qualitatively speaking, this suggests the use of at least two sensors per (micro-seismic) source. When using S sensors in a laboratory setting, one should accordingly expect to reliably reconstruct up to $S/2$ simultaneous sources. In situations where the reconstruction algorithm consistently exposes more than $S/2$ contemporaneous events, the above result suggests either (i) deploying additional motion sensors, or (ii) retaining only the "strongest" $S/2$ events, as quantified e.g. in terms of Frobenius norm of the moment tensors M_i, $i = 1, 2, \ldots, N$. For completeness, we note that in conventional acoustic emission (AE) testing [Grosse and Ohtsu, 2008], micro-seismic events are reconstructed one at a time, which precludes the existence of contemporaneous sources.

3.2 Example 2

In this second and last example, we examine the robustness of the reconstruction algorithm with respect to random modeling errors. To this end, we assume the true material parameters to be corrupted with White Gaussian Noise according to

$$\mu_\tau = \mu(1 + \tau\varphi) \ , \quad \lambda_\tau = \lambda(1 + \tau\varphi) \quad \text{and} \quad \rho_\tau = \rho(1 + \tau\varphi) \ , \tag{32}$$

where $\varphi : \Omega \mapsto (0, 1)$ is a random variable and τ specifies the amplitude of fluctuations. The domain Ω is subdivided into 10×10 subregions. To have a meaningful representation of material heterogeneities, each subregion is discretized by 4^4 triangular elements where the corrupted material parameters are evaluated according to (32). In this way, the average heterogeneity size d_h can be computed as $d_h/\lambda_s = (5/10)/4^2 \simeq 0.03$, i.e. 3% of the shear wavelength. For consistency, such material distribution is then projected onto a finer mesh with 4^7 triangular elements per subregion, leading to a finite element discretization that is commensurate with those in the former example. As before, the reconstruction algorithm assumes a homogeneous background model with Lamé parameters $\lambda = \mu$ and mass density ρ. The perturbation function $(1 + \tau\varphi)$ is plotted in Fig. 5 with $\tau = 1$. For completeness of discussion, we next introduce the effective noise level in the data due to (32) as

$$\tau^\star := \frac{\|u_0 - u_\tau\|_{L^2(\Omega)}}{\|u_0\|_{L^2(\Omega)}}, \tag{33}$$

where $u_0 = u_{\tau|_{\tau=0}}$ and u_τ is the acoustic emission field due to exact source distribution (5) computed assuming (32) for the background solid.

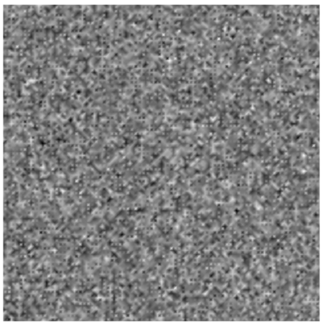

Figure 5: Corrupted background with White Gaussian Noise.

In this scenario, let us reconstruct a single mode II event with $\bar{\gamma}_1 = 0.05$ and $\theta_1 = 15°$ using the six sensors shown in Fig. 6. We assume that the number of faults is not known, and we set $N = 2 > N^* = 1$. The results of source reconstruction for 0.5%, 1.0% and 2.0% are shown in Fig. 6. For $\tau = 0.0\%$, the reconstruction is nearly exact and thus the result is not reported. For $\tau = 0.5\%$ ($\tau^\star = 10\%$), the reconstruction is still good, but there is a minuscule artifact in the form of a *phantom* second event as permitted by the premise $N = 2$. This type of solution degradation continues to grow for $\tau = 1.0\%$ ($\tau^\star = 21\%$) and $\tau = 2.0\%$ ($\tau^\star = 51\%$) as can be seen from the respective displays.

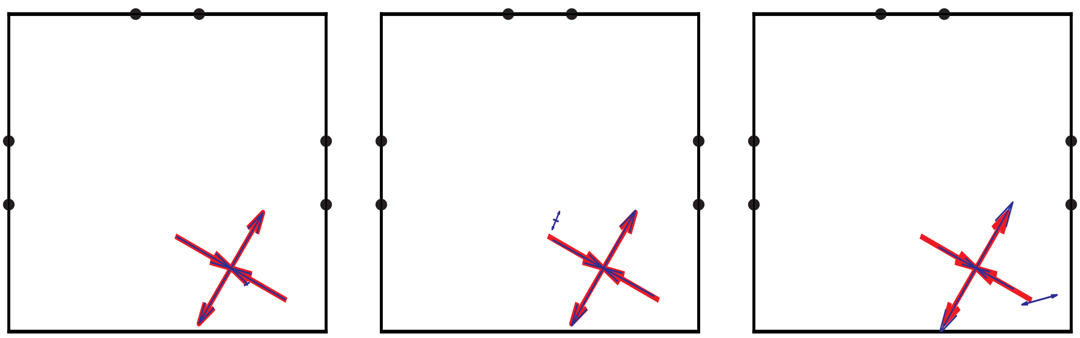

(a) $\tau = 0.5\%$ ($\tau^\star = 10\%$) (b) $\tau = 1.0\%$ ($\tau^\star = 21\%$) (c) $\tau = 2.0\%$ ($\tau^\star = 51\%$)

Figure 6: Reconstruction of a single micro-fault under varying levels of noise.

4 Concluding Remarks

In this study, we propose an algorithm for the frequency-domain reconstruction of micro-seismic events using full-waveform analysis of the acoustic emission data. The inversion approach integrates a combinatorial grid search for source locations with the sensitivity analysis in terms of moment tensor components to arrive at an effective algorithm that simultaneously returns both micro-seismic source coordinates and respective tensorial strengths. We investigate the performance of the algorithm, assuming pointwise wave-form observations, via numerical examples that include both isolated and multiple point sources. Under ideal testing conditions, the results suggest that two point receivers per acoustic emission source may provide sufficient information for accurate moment tensor inversion. For generality, we also investigate the micro-seismic source reconstruction under the adverse condition of randomly perturbed background medium, whose local fluctuations are unavailable as prior information. The results show a significant resilience of the reconstruction algorithm to this type of modeling errors.

Acknowledgements

This research was partly supported by CNPq (Brazilian Research Council) and FAPERJ (Research Foundation of the State of Rio de Janeiro). These financial support are gratefully acknowledged.

References

K. Aki and P. Richards. *Quantitative Seismology*. University Science Books, Sausalito, California, 2009.

G. Allaire, F. Jouve, and N. Van Goethem. Damage and fracture evolution in brittle materials by shape optimization methods. *Journal of Computational Physics*, 230(12): 5010–5044, 2011.

A. Amad, A. Novotny, and B. Guzina. On the full-waveform inversion of seismic moment tensors. *International Journal of Solids and Structures*, 202(1):717–728, 2020. doi: 10.1016/j.ijsolstr.2020.06.012.

S. Amstutz. An introduction to the topological derivative. *Engineering Computations*, 39 (1):3–33, 2022.

S. Amstutz and A. Novotny. Topological optimization of structures subject to von Mises stress constraints. *Structural and Multidisciplinary Optimization*, 41(3):407–420, 2010.

S. Amstutz, S. Giusti, A. Novotny, and E. de Souza Neto. Topological derivative for multi-scale linear elasticity models applied to the synthesis of microstructures. *International Journal for Numerical Methods in Engineering*, 84:733–756, 2010.

S. Amstutz, A. Novotny, and N. Van Goethem. Minimal partitions and image classification using a gradient-free perimeter approximation. *Inverse Problems and Imaging*, 8 (2):361–387, 2014.

D. Auroux, L. J. Belaid, and M. Masmoudi. A topological asymptotic analysis for the regularized greylevel image classification problem. *ESAIM Mathematical Modelling and Numerical Analysis*, 41:607–625, 2007.

A. Baig and T. Urbancic. Microseismic moment tensors: A path to understanding frac growth. *The Leading Edge*, 29:320–324, 2010.

G. Barros, J. Filho, L. Nunes, and M. Xavier. Experimental validation of a topological derivative-based crack growth control method using digital image correlation. *Engineering Computations*, 39(1):438–454, 2022.

P. Baumann and K. Sturm. Adjoint-based methods to compute higher-order topological derivatives with an application to elasticity. *Engineering Computations*, 39(1):60–114, 2022.

F. Bazargani and R. Snieder. Optimal source imaging in elastic media. *Geophysical Journal International*, 204:1134–1147, 2015.

M. Bonnet. On the justification of topological derivative for wave-based qualitative imaging of finite-sized defects in bounded media. *Engineering Computations*, 39(1):313–336, 2022.

A. Canelas and J. Roche. Shape and topology optimal design problems in electromagnetic casting. *Engineering Computations*, 39(1):147–171, 2022.

A. Canelas, A. Laurain, and A. Novotny. A new reconstruction method for the inverse potential problem. *Journal of Computational Physics*, 268:417–431, 2014.

A. Canelas, A. Laurain, and A. Novotny. A new reconstruction method for the inverse source problem from partial boundary measurements. *Inverse Problems*, 31(7):075009, 2015. doi: 10.1088/0266-5611/31/7/075009.

S. Cesca and T. Dahm. A frequency domain inversion code to retrieve time-dependent parameters of very long period volcanic sources. *Computers & Geosciences*, 34:235–246, 2008.

M. Delfour. Topological derivatives via one-sided derivative of parametrized minima and minimax. *Engineering Computations*, 39(1):34–59, 2022.

L. Fernandez and R. Prakash. Imaging of small penetrable obstacles based on the topological derivative method. *Engineering Computations*, 39(1):201–231, 2022.

A. Ferreira and A. Novotny. A new non-iterative reconstruction method for the electrical impedance tomography problem. *Inverse Problems*, 33(3):035005, 2017. doi: 10.1088/1361-6420/aa54e4.

A. Ferrer and S. Giusti. Inverse homogenization using the topological derivative. *Engineering Computations*, 39(1):337–353, 2022.

S. Garreau, P. Guillaume, and M. Masmoudi. The topological asymptotic for PDE systems: the elasticity case. *SIAM Journal on Control and Optimization*, 39(6):1756–1778, 2001.

F. Gilbert. Derivation of source parameters from low-frequency spectra. *Philosophical Transactions of the Royal Society of London. Series A, Mathematical and Physical Sciences*, 274:369–371, 1973.

S. Giusti, A. Novotny, and E. de Souza Neto. Sensitivity of the macroscopic response of elastic microstructures to the insertion of inclusions. *Proceeding of the Royal Society A: Mathematical, Physical and Engineering Sciences*, 466:1703–1723, 2010.

C. Grosse and M. Ohtsu. *Acoustic Emission Testing*. Springer Science & Business Media, 2008.

M. Jost and R. Herrmann. A student's guide to and review of moment tensors. *Seismological Research Letters*, 60:37–57, 1989.

H. Kawakatsu and J. Montagner. Time-reversal seismic-source imaging and moment-tensor inversion. *Geophysical Journal International*, 175:686–688, 2008.

P. Kliewe, A. Laurain, and K. Schmidt. Shape optimization in acoustic-structure interaction. *Engineering Computations*, 39(1):172–200, 2022.

R. Koerner, W. McCabe, and A. Lord. Overview of acoustic emission monitoring of rock structures. *Rock Mechanics*, 14:27–35, 1981.

F. L. Louër and M. Rapún. Topological sensitivity analysis revisited for time-harmonic wave scattering problems. Part I: The free space case. *Engineering Computations*, 39 (1):232–271, 2022a.

F. L. Louër and M. Rapún. Topological sensitivity analysis revisited for time-harmonic wave scattering problems. Part II: Recursive computations by the boundary integral equation method. *Engineering Computations*, 39(1):272–312, 2022b.

A. Novotny and J. Sokołowski. *Topological derivatives in shape optimization*. Interaction of Mechanics and Mathematics. Springer-Verlag, Berlin, Heidelberg, 2013. doi: 10.1007/978-3-642-35245-4.

A. Novotny and J. Sokołowski. *An introduction to the topological derivative method*. Springer Briefs in Mathematics. Springer Nature Switzerland, 2020. doi: 10.1007/978-3-030-36915-6.

A. Novotny, R. Feijóo, E. Taroco, and C. Padra. Topological sensitivity analysis for three-dimensional linear elasticity problem. *Computer Methods in Applied Mechanics and Engineering*, 196(41–44):4354–4364, 2007.

A. Novotny, J. Sokołowski, and A. Żochowski. *Applications of the topological derivative method*. Studies in Systems, Decision and Control. Springer Nature Switzerland, 2019a. doi: 10.1007/978-3-030-05432-8.

A. Novotny, J. Sokołowski, and A. Żochowski. Topological derivatives of shape functionals. Part III: Second order method and applications. *Journal of Optimization Theory and Applications*, 181(1):1–22, 2019b.

A. Novotny, S. Giusti, and S. Amstutz. Guest Editorial: On the topological derivative method and its applications in computational engineering. *Engineering Computations*, 39(1):1–2, 2022.

L. Rakotondrainibe, G. Allaire, and P. Orval. Topological sensitivity analysis with respect to a small idealized bolt. *Engineering Computations*, 39(1):115–146, 2022.

A. Romero. Optimum design of two-material bending plate compliant devices. *Engineering Computations*, 39(1):395–420, 2022.

R. Santos and C. Lopes. Topology optimization of structures subject to self-weight loading under stress constraints. *Engineering Computations*, 39(1):380–394, 2022.

A. Schumacher. *Topologieoptimierung von bauteilstrukturen unter verwendung von lochpositionierungkriterien*. Ph.D. Thesis, Universität-Gesamthochschule-Siegen, Siegen - Germany, 1995.

C. Scruby, G. Baldwin, and K. Stacey. Characterisation of fatigue crack extension by quantitative acoustic emission. *International Journal of Fracture*, 28:201–222, 1985.

P. Shearer. *Introduction to Seismology*. Cambridge University Press, 2009.

B. Sjögreen and N. Petersson. Source estimation by full wave form inversion. *Journal of Scientific Computing*, 59(1):247–276, 2014.

J. Sokołowski and A. Żochowski. On the topological derivative in shape optimization. *SIAM Journal on Control and Optimization*, 37(4):1251–1272, 1999.

F. Song and M. Toksöz. Full-waveform based complete moment tensor inversion and source parameter estimation from downhole microseismic data for hydrofracture monitoring. *Geophysics*, 76:WC103–WC116, 2011.

M. Xavier and N. Van Goethem. Brittle fracture on plates governed by topological derivatives. *Engineering Computations*, 39(1):421–437, 2022.

M. Xavier, E. Fancello, J. Farias, N. Van Goethem, and A. Novotny. Topological derivative-based fracture modelling in brittle materials: A phenomenological approach. *Engineering Fracture Mechanics*, 179:13–27, 2017.

R. Yera, L. Forzani, C. Méndez, and A. Huespe. A topology optimization algorithm based on topological derivative and level-set function for designing phononic crystals. *Engineering Computations*, 39(1):354–379, 2022.